Journal of Materials Chemistry A

Accepted Manuscript

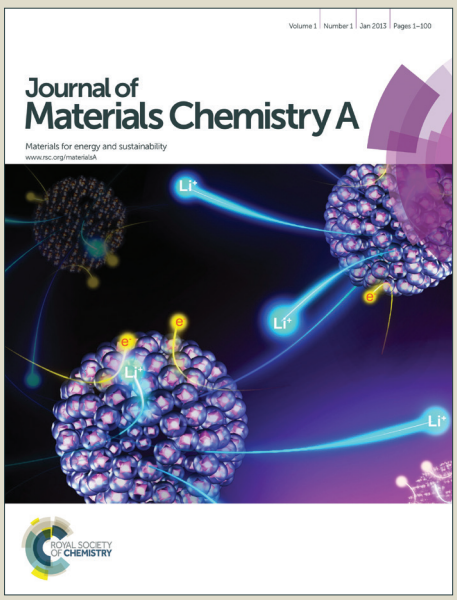

ROYAL SOCIETY OF CHEMISTRY

www.rsc.org/materialsA

Theoretical Design of MoO_3-Based High-Rate Lithium Ion Battery Electrodes: The Effect of Dimensionality Reduction

Fengyu Li,[a] Carlos R. Cabrera,[b] Zhongfang Chen[a,*]

[a] Department of Chemistry, [b] NASA-URC Center of Advanced Nanoscale Materials, University of Puerto Rico, Rio Piedras Campus, PO Box 23346, San Juan, PR 00931, USA

To whom correspondence should be addressed. Email: zhongfangchen@gmail.com (ZC)

Abstract

By means of density functional theory computations, we systematically investigated the behavior of lithium (Li) adsorption and diffusion on MoO_3 with different dimensions: including three-dimensional (3D) bulk, two-dimensional (2D) double-layer, 2D monolayer and one-dimensional (1D) nanoribbons. The Li binding energies and diffusion barriers are comparable in MoO_3 bulk and double-layer. Reducing the dimension to MoO_3 monolayer simultaneously lowers the Li diffusion barrier and the interaction between Li atoms and MoO_3 monolayer. Cutting MoO_3 monolayer into 1D nanoribbons can further facilitate the diffusion of Li atoms, and enhance the Li binding energies. Especially, Li diffusion on nanoribbons is rather facile along both the axial and the transverse directions. These computational results demonstrate that due to the dimensional reduction, MoO_3 monolayer nanosheets and nanoribbons have exceptional properties (good electronic conductivity, fast Li diffusion, high operating voltage and high energy density), thus are promising as high-rate Li ion battery electrodes.

Keyword: Molybdenum oxide, two-dimensional structures, nanoribbons, cathode materials, lithium ion batteries, density functional calculations.

TOC

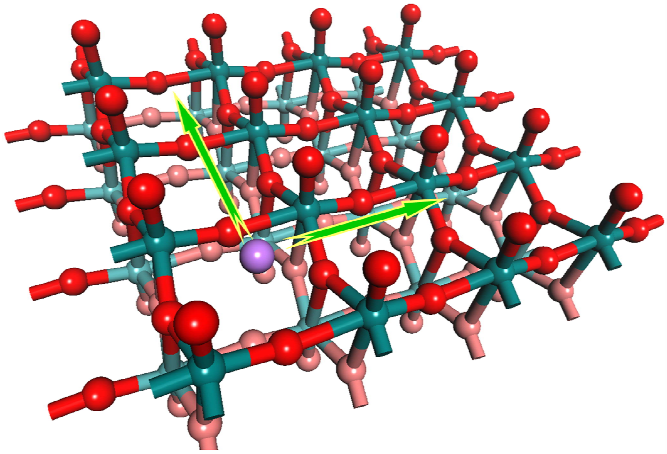

1. Introduction

Electrochemical energy storage devices are indispensable in solving environmental and sustainability problems associated with fossil fuels.[1,2] Among them, rechargeable lithium-ion batteries (LIBs) have been widely used from portable electronics to electric vehicles and grid storage. However, the further success of LIBs technology depends on the development of new electrode materials with superior electrochemical properties that can offer higher energy and power density at an affordable cost and acceptable safety.

Layered metal oxides/sulfides, such as V_2O_5,[3,4] MoO_3,[5] MoS_2,[6] SnS_2,[7] with strong intralayer covalent bonding and weak van der Waals coupling between layers, are usually used as cathodes,[8] since the layers provide more opportunities of intercalation and good mobility for the electrolyte ions, which leads to a better utilization of the high surface area offered by the layers.

Molybdenum oxide (MoO_3), whose crystal structure of α-MoO_3 was first determined in 1931,[9] has a layered orthorhombic arrangement with space group of *Pnma,* and contains four formula units of MoO_3 per unit cell. The MoO_3 single sheet adopts a bilayer structure with both sides of surface terminated with oxygen atoms O1; the intralayer is bridge-connected by oxygen (O2) along (100) direction (*a*-axis direction in Figure 1) and corner-linked along (001) direction (*c*-axis direction in Figure 1); the interlayer is combined by the Mo-O bonds where O is tri-coordinated (O3), and the interlayer Mo-O bonds are almost perpendicular to the layer surface.

Because of these structural characteristics, MoO_3 has been extensively employed as LIB cathode materials, which can deliver the capacities of 200–400 mA h g^{-1} between 1.5 and 3.6 V via an intercalation mechanism.[10-20] Low-dimensional α-MoO_3 nanostructures, fabricated by a variety of experimental routes, have been

used as efficient LIBs electrode materials, since the dimension reduction from bulk to nanoscale can help release the huge stresses and strains, accommodate the volume change, and increase the intercalation rate during charging/discharging. For example, MoO_3 nanoparticles, [21] MoO_3 nanorods,[15, 22] MoO_{3-x} nanowire arrays [23] and carbon-coated MoO_3 nanobelts[24] were found to be stable and of enhanced lithium storage capabilities; MoO_3 thin films exhibit high-rate Li-ion intercalation;[25,26] as a cathode material, MoO_3 nanobelts show higher capacity and better cycle ability in the high rate performance over bulk α-MoO_3.[13,14,18] Because of the improved performance of these nanomaterials, we expect that MoO_3 monolayer nanosheets and nanoribbons may be used as promising cathode materials for high performance rechargeable batteries.

In this work, we systemically investigated the adsorption and diffusion properties of single Li atom on three-dimensional (3D) bulk, two-dimensional (2D) double/single-layer and one-dimensional (1D) nanoribbon of MoO_3, as well as their lithium storage capacity by means of density functional theory (DFT) in order to gain insights into the performance of the MoO_3 monolayer nanosheets and nanoribbons as LIB cathodes. Binding energies (E_b) and diffusion energy barriers (E_d) are two important factors that affect electrochemical performance.[2] A larger positive adsorption energy indicates a more favorable exothermic lithiation reaction between cathode materials and lithium, and Li will diffuse at a faster rate if the diffusion energy barrier is reduced. Our studies showed that double-layer MoO_3 has comparable Li binding energy and Li diffusion barrier as the bulk MoO_3, monolayer has simultaneously decreased binding energy and diffusion barrier; dimension reduction to nanoribbons further lowers the Li diffusion barriers along certain routes, while enhances Li binding energies compared to monolayer, even to bulk. The above results

indicate that MoO_3 monolayer and nanoribbons are promising as cathode materials for Li-ion batteries with a high power density and fast charge–discharge rates, highlighting the importance of dimension reduction for designing LIB cathodes.

2. Computational Methods

All density functional theory (DFT) computations were performed by using the plane-wave technique as implemented in the Vienna *ab initio* simulation package (VASP).[3] The ion–electron interaction is described with the projector augmented wave (PAW) method.[4] A 500 eV cutoff was used for the plane-wave basis set. The exchange-correlation energy is described by the functional of Perdew, Burke, and Ernzerhof (PBE).[5] To investigate single Li adsorption and diffusion in the MoO_3-based nanostructures, the bulk/double-layer/monolayer (nanoribbon) was modeled in a 3 × 3 × 1 (3 × 1 × 1) lateral supercell and separated by 12 Å of vacuum. The geometry optimizations were performed by using the conjugated gradient method, and the convergence threshold was set to be 10^{-4} eV in energy and 10^{-3} eV/Å in force. The Brillouin zone was represented by Monkhorst–Pack special k-point mesh of 4 × 8 × 4, 4 × 4 × 1 and 4 × 1 × 1 for three-dimensional (3D) bulk, two-dimensional (2D) sheets and one-dimensional (1D) ribbons, respectively. The PBE-D2 method,[6] which introduces dispersion interactions by using an empirical potential of the form C_6R^{-6}, was adopted for the geometry optimization of bulk and double-layer. Furthermore, the climbing-image nudged elastic band (CI-NEB) method[7] implemented in VASP was used to determine the diffusion energy barriers and the minimum energy pathways for Li diffusion in the bulk/double-layers and on the monolayer sheet/nanoribbons.

In our study, the Li binding energy, E_b, is defined as $E_b = E(MoO_3) + E(Li) - E(Li\text{-}MoO_3)$, where $E(Li\text{-}MoO_3)$, $E(MoO_3)$, and $E(Li)$ are the total energies of

Li-adsorbed MoO_3 (bulk, double-layer, and monolayer sheet/nanoribbon), the energy of an isolated Li atom, and the energy of pristine MoO_3, respectively. According to this definition, a more positive binding energy indicates a more favorable exothermic lithiation reaction between MoO_3 and Li atoms.

3. Results and Discussion

3.1. Li adsorption and diffusion in bulk MoO_3 and 2D double-layers.

We first examined the adsorption and diffusion of Li atom in the bulk phase of MoO_3. A 3×3×1 supercell for MoO_3 bulk was used, which consists of 36 Mo atoms and 108 O atoms. Two possible sites for lithiation in MoO_3 bulk are: (1) **O1H** at which Li sits at the hollow site of one layer pointing to the terminal O1 of the adjacent layer (Figure 1b); (2) **O2O3** at which Li locates between the bridge oxygen O2 of one layer and the tri-coordinated oxygen O3 of the other layer and is surrounded by four surface terminal O1 atoms (Figure 1a,c).

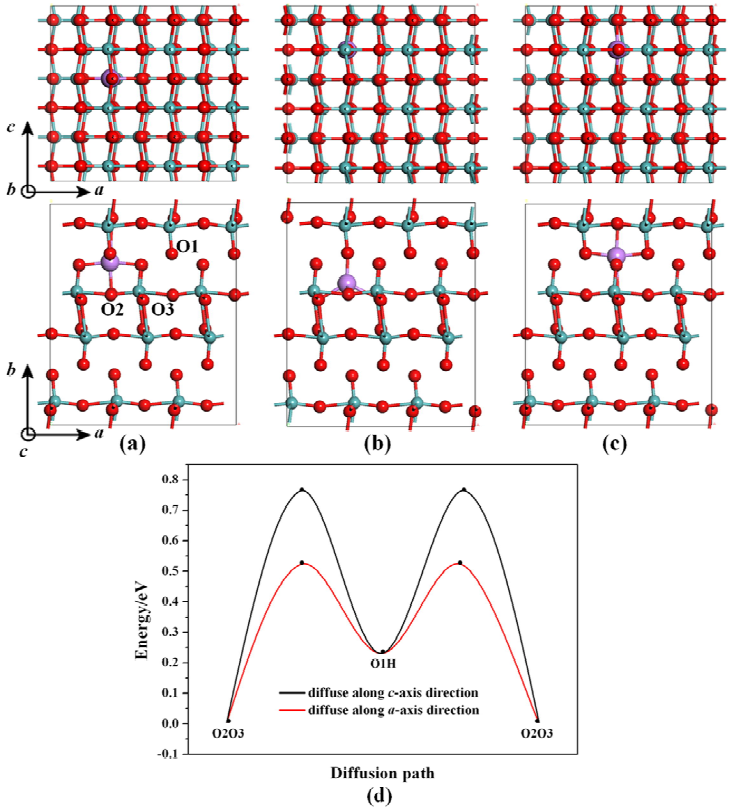

Figure 1. Top (upper panel) and two side (middle and lower panels) views of the optimized geometries with a Li atom adsorbed at the **O2O3** site (a, c), and **O1H** site (b) of MoO_3 bulk. The cyan, red, and pink balls denote Mo, O and Li atoms, respectively. (d) Energy profiles for Li diffusion in MoO_3 bulk between two **O2O3** sites through an **O1H** site along *a*-axis (red curve) and *c*-axis (black curve) directions, respectively.

Our computations showed that Li atom prefers to adsorb at the **O2O3** site (Figure 1a,c) with a binding energy of 4.15 eV, the newly formed Li-O bonds are in the range of 1.94~2.03 Å. The lithium adsorption at the **O1H** site (Figure 1b) is also energetically favorable (with a binding energy of 3.92 eV); in this case, the newly formed Li-O bonds between Li and O around the hollow site in the same layer are 1.94~2.25 Å, and the distance between Li and the terminal O is 1.94 Å.

Furthermore, we studied the Li atom diffusion in MoO_3 bulk between two neighboring **O2O3** sites, passing through an **O1H** site along both *a*-axis and *c*-axis directions (Figure 1d). The computed diffusion barriers are 0.76 and 0.53 eV, respectively, indicating that Li atoms can relatively well diffuse in bulk MoO_3, and Li atoms prefer to diffuse along *c*-axis.

As a comparison, we also studied the Li adsorption and diffusion in MoO_3 2D double-layers. The interlayer surface-oxygen distance of double-layer (2.79 Å) is slightly larger than that (2.78 Å) in the bulk phase. As a consequence, the Li-O bonds are slightly longer (1.94~2.04 Å and 1.95~2.25 Å at **O2O3** and **O1H** sites, respectively) than those in MoO_3 bulk. The E_b values of Li at **O2O3** and **O1H** sites are 4.14 and 3.91 eV, respectively, almost the same as those in bulk phase. The diffusion barriers (E_d) of Li from **O2O3** site to **O1H** position, 0.74 and 0.51 eV along *a*-axis and *c*-axis directions, respectively, are also comparable to those in the bulk.

Thus, reducing the dimension from 3D bulk to 2D double-layer does not bring any significant effect on the Li binding energies or diffusion barriers. Though Li can well diffuse in 3D bulk and 2D double-layer, to further increase the Li mobility, the diffusion barrier needs to be lowered. It is expected that Li can diffuse faster on the MoO_3 monolayer/nanoribbons since some hindrance can be avoided.

3.2. Li adsorption and diffusion on 2D MoO_3 monolayer.

2D atomic crystals typically possess larger surface volume ratio compared to their 3D bulk counterparts, providing more sites for lithium adsorption. For example, theoretical studies have demonstrated that Ti_3C_2, [27] B/N-doped graphene, [28] Li_4NiTeO_6, [29] BSi_3 silicene [30] and VS_2 monolayer [31] are promising electrodes for lithium-ion batteries. Recently, the impressive experimental and theoretical progress

on graphene-analogous low-dimensional materials (2D nanosheets and 1D nanoribbons) and their applications for lithium ion batteries have been thoroughly reviewed.[3233] In this section, we explored the behavior of lithium adsorption and diffusion on 2D MoO_3 monolayer.

On MoO_3 monolayer (Figure 2a), the bridge-oxygen site (**O2**) is most favorable for lithiation (E_b = 4.09 eV), slightly larger than that at the **O3** site (E_b = 4.06 eV). The Li binding strength at the hollow site (**H**) is comparable to that at the **O2** site (4.05 eV), while the terminal oxygen site (**O1**) is less favorable (E_b = 3.58 eV). Different to the pronounced reduced Li binding upon the dimension reduction from 3D to 2D in the C_3B[34] and MoS_2[6] materials, the highest Li binding energy in MoO_3 monolayer is only 0.06 eV lower than that for the most favorable site in MoO_3 bulk (4.15 eV), which originates from the shortened Li-O bond lengths in the monolayer (see Table 1) compared to bulk, though the Li coordination is reduced.

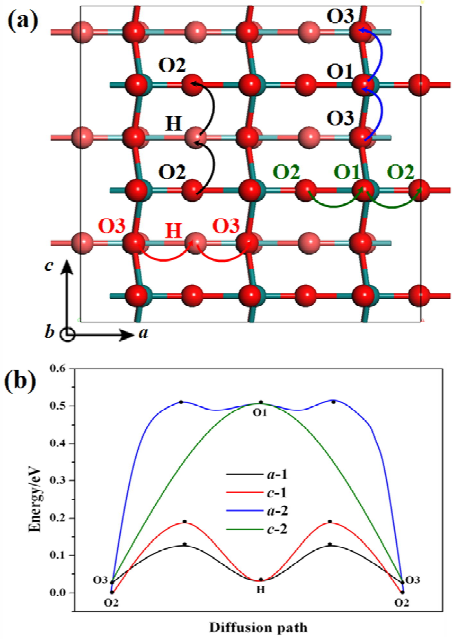

Figure 2. (a) Various Li adsorption sites in a MoO_3 monolayer, and possible Ii diffusion routes. The cyan (light cyan) and red (light red) balls denote Mo and atoms of the first (second) layer, respectively. (b) Energy profiles for Li diffusion on MoO_3 monolayer in different routes, the energy of **O2** site was set as zero.

We examined four possible diffusion routes for Li on MoO_3 monolayer (Figure 2a), namely, migrating along *a*-axis direction: Route *a*-1 (**O3→H→O3**) and Route *a*-2 (**O2→O1→O2**); migrating along *c*-axis direction: Route *c*-1 (**O2→H→O2**) and Route *c*-2 (**O3→O1→O3**). The corresponding diffusion barriers (0.11 and 0.10, 0.20 and 0.16, 0.52 and 0.01, 0.48 and 0.00 eV, respectively, Figure 2b) are dramatically lower than the diffusion barriers in the bulk phase (0.53 and 0.76 eV) and double layer (0.51 and 0.74 eV). The Li atom is apt to diffuse from one **O3** (**O2)** site to another passing through a **H** site along *a*-axis (*c*-axis) direction, the diffusion barriers are rather low, 0.11 and 0.01 (0.20 and 0.16) eV.

3.3. Li adsorption and diffusion on MoO_3 nanoribbons (NRs)

Cutting 2D materials into 1D nanostructures may change the electronic and magnetic properties due to the edge effect, and thus it may alternate the behavior of Li adsorption and diffusion. Inspired by previous findings that cutting graphene or MoS_2 nanosheets into 1D nanoribbons can significantly enhance the Li binding energies,[35,6] we expected that the enhanced Li binding could also exist in MoO_3 NRs. In this section, we focus on the adsorption and diffusion of Li atoms on the MoO_3 NRs. Notably, in our previous work, we found that the MoO_3 NRs cut along *c*-axis with even number width (*c-Ne*) and with both edges terminated by alternative projecting-oxygen have the smallest edge formation energies (E_{EF}) among all the nanoribbons, and the MoO_3 NRs cut along *a*-axis with odd number width (*a-No*) also have small E_{EF} values.[36] Therefore, we chose *12-c* and *11-a* MoO_3 NRs as the models to study the Li adsorption and diffusion on the MoO_3 NRs. Here the $1 \times 1 \times 3$ and $3 \times 1 \times 1$ supercells with one adsorbed Li atom were used to investigate the Li adsorption, which correspond to a chemical stoichiometry of $Mo_{36}O_{108}Li$ and $Mo_{33}O_{99}Li$, respectively. In the following section, we will first discuss the Li adsorption and diffusion on *12-c* NR, then on *11-a* MoO_3 NR.

MoO_3 bulk, monolayer and nanoribbons were characterized as a wide band semiconductors,[36] recent DFT study showed that the lithium inserted α-MoO_3 bulk are metals,[37] and our calculations demonstrated that the single-Li-intercalated *12-c* and *11-a* NRs also exhibit metallic behavior (Figure S1).

12-c NR.

In lack of symmetry, many unique sites for lithiation are available along the

periodic direction of 12-*c* MoO_3 NR (*c*-axis direction). In this study, we considered all the possible sites throughout the ribbon for Li adsorption on *12-c* MoO_3 NR, including five **O2** sites (**$O2_1$–$O2_5$**), six **O3** sites (**$O3_1$–$O3_6$**), five **H** sites (**H_1–H_5**), and six **O1** sites (**$O1_1$–$O1_5$**) on the basal plane, and three sites on the side plane (**E_1–E_3**), as shown in Figure 3.

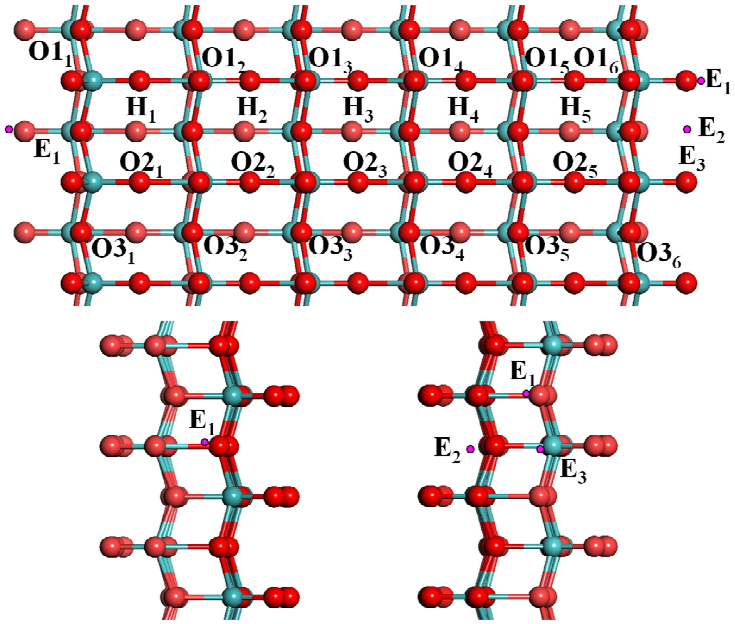

Figure 3. Top and side views of geometry of *12-c* MoO_3 NR. All the examined Li adsorption sites are denoted with black characters. The cyan (light cyan) and red (light red) balls denote Mo and atoms of one (the other) sublayer, respectively. The pink dots represent the edge adsorption sites.

The computed Li binding energies (E_b) and average Li-O bond distances ($d_{Li\text{-}O}$) of all the examined sites for *12-c* MoO_3 NR were summarized in Table 1. For the **H** sites, Li atoms locate off the hollow center and bind two adjacent surface oxygen O1

atoms along *c*-axis. For the **O2** (**O3**) sites, Li sits over the O2 (O3) atoms binding with the two adjacent O1 atoms. For the edge sites, at $\mathbf{E_1}$ site Li is bonded with one projecting oxygen and one edge O3 atom, at $\mathbf{E_2}$ site Li sits between two projecting oxygen, and at $\mathbf{E_3}$ site Li locates over Mo bonded with two projecting oxygen and one surface oxygen.

Table 1. Computed Li binding energies (E_b) and average Li-O bond distances ($d_{Li\text{-}O}$) of all the examined Li adsorption sites for *12-c* MoO_3 NR.

	12-c NR						monolayer
Site	$\mathbf{H_1}$	$\mathbf{H_2}$	$\mathbf{H_3}$	$\mathbf{H_4}$	$\mathbf{H_5}$		**H**
E_b/eV	3.63	3.83	3.91	4.01	4.11		4.05
$d_{Li\text{-}O}$/Å	2.46	2.19	2.22	2.18	2.21		1.90
Site	$\mathbf{O2_1}$	$\mathbf{O2_2}$	$\mathbf{O2_3}$	$\mathbf{O2_4}$	$\mathbf{O2_5}$		**O2**
E_b/eV	3.50	3.86	3.97	4.05	4.14		4.06
$d_{Li\text{-}O}$/Å	1.93	2.06	2.01	2.00	1.99		1.91
Site	$\mathbf{O3_1}$	$\mathbf{O3_2}$	$\mathbf{O3_3}$	$\mathbf{O3_4}$	$\mathbf{O3_5}$	$\mathbf{O3_6}$	**O3**
E_b/eV	3.72	3.84	3.95	4.01	4.03	4.04	4.09
$d_{Li\text{-}O}$/Å	1.87	1.87	1.88	1.88	1.88	1.87	1.88
Site	$\mathbf{O1_1}$	$\mathbf{O1_2}$	$\mathbf{O1_3}$	$\mathbf{O1_4}$	$\mathbf{O1_5}$	$\mathbf{O1_6}$	**O1**
E_b/eV	3.15	3.36	3.44	3.49	3.53	3.45	3.59
$d_{Li\text{-}O}$/Å	1.74	1.75	1.75	1.75	1.75	1.75	1.76
Site	$\mathbf{E_1}$	$\mathbf{E_2}$	$\mathbf{E_3}$				
E_b/eV	3.29	4.14	3.81				
$d_{Li\text{-}O}$/Å	1.93	1.83	1.99				

The Li binding energies of all the considered adsorption sites for *12-c* MoO_3 NR are in the range of 3.15~4.14 eV, much higher than the cohesive energy (1.56 eV from our calculation) per Li in bulk Li, thus excluding the phase separation and formation of hazardous Li dendrites.[38] Among all the considered adsorption sites, the two-fold edge site $\mathbf{E_2}$ and the three-fold $\mathbf{O2_5}$ site in the edge region have the highest Li binding energy (both 4.14 eV), followed by the edge hollow site $\mathbf{H_5}$ (4.11 eV). The Li binding energies increase from the O3 terminated edge side to the oxygen-projecting ended

edge side for **H**, **O2** and **O1** series of adsorption sites (Table 1), implying the considerable edge effect. The sites close to the oxygen-projecting edge have comparable Li binding energies (4.11~4.14 eV) to those in bulk (4.15 eV) and slightly higher bind strength than those on the MoO_3 monolayer sheet (4.05~4.09 eV). The Li binding energies on *12-c* MoO_3 NR are also larger than those on zigzag MoS_2 nanoribbons.[6]

To examine the effect of dimension reduction on the Li mobility, we then investigated the Li diffusion behavior along different pathways in both periodic (*c*-axis) and transverse (*a*-axis) directions of *12-c* MoO_3 NR. Due to the asymmetrical structural property, various diffusion pathways have to be considered. For the diffusion routes along the periodic direction (*c*-axis), we examined the Li diffusion from $\mathbf{O3}_i$ site to $\mathbf{O1}_i$ site (i = 1−6) (termed P_{O3O1}-i), from $\mathbf{O2}_i$ site to $\mathbf{H}_i$ site (i = 1−5) (termed P_{O2H}-i), from $\mathbf{E_2}$ to $\mathbf{E_2}$ (P_{E2E2}), from $\mathbf{E_1}$ to $\mathbf{E_2}$ (P_{E1E2}), and from $\mathbf{E_1}$ to $\mathbf{E_3}$ (P_{E1E3}); for the pathways along the transverse direction (*a*-axis), we examined the Li diffusion from $\mathbf{O3}_i/\mathbf{O3}_{i+1}$ site to $\mathbf{H}_i$ site (i = 1−5) (termed T_{O3H}-i), from $\mathbf{O2}_{\_i}$ site to $\mathbf{O1}_i/\mathbf{O1}_{i+1}$ site (i = 1−5) (termed T_{O2O1}-i), from $\mathbf{O3}_{\_1}$ to $\mathbf{E_1}$ (T_{O3E1}), from $\mathbf{O3}_{\_6}$ to $\mathbf{E_2}$(T_{O3E2}), and from $\mathbf{E_2}$ to $\mathbf{E_3}$ (T_{E2E3}).

For Li diffusion along the periodic direction (as illustrated in Figure 4), it is kinetically more favorable for Li to migrate through P_{O2H}-i (i = 1−5) channels (blue routes in Figure 4), the diffusion barriers are between 0.08 and 0.25 eV, and P_{O2H}-2 has the lowest diffusion barriers (0.08 and 0.13 eV) among the five P_{O2H} routes, while the barriers of P_{O2H}-5 route (0.21 and 0.24 eV), where the $\mathbf{O2_5}$ has the strongest Li

binding energy, are higher than those of similar diffusion route on MoO_3 monolayer (0.14 and 0.15 eV); despite it is energy barrierless for Li diffusing from $\mathbf{O1}_i$ site to $\mathbf{O3}_i$ site (P_{O3O1}-i, i = 1–6), the barrier of migrating from $\mathbf{O3}_i$ site to $\mathbf{O1}_i$ site is rather high (0.48~0.59 eV, black routes in Figure 4); it is energy-demanding for Li diffusion in the edge plane along *c*-axis (green routes in Figure 4): the barriers of Li migration from $\mathbf{E_3}$ to $\mathbf{E_1}$ and from one $\mathbf{E_2}$ site to another $\mathbf{E_2}$ site (route P_{E2E2}) are 0.66 and 0.81 eV, respectively; and even higher energy barrier (1.05 eV) has to be overcome from $\mathbf{E_2}$ site to $\mathbf{E_1}$ site (route P_{E1E2}) for Li moving on the edge plane.

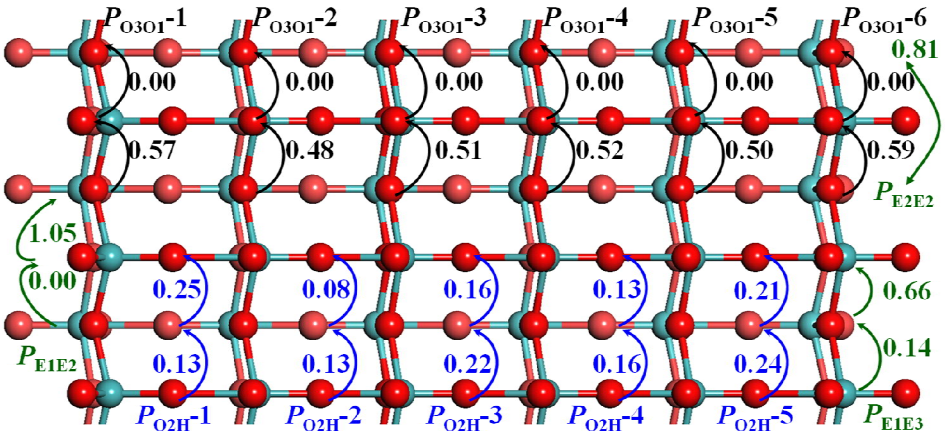

Figure 4. Top view of Li diffusion pathways on *12-c* MoO_3 NR along the periodic direction. The numbers indicate the diffusion barriers in eV. The cyan (light cyan) and red (light red) balls denote Mo and atoms of one (the other) sublayer, respectively.

For Li diffusing along transverse (*a*-axis) direction on the basal plane of *12-c* MoO_3 NR, it is more feasible for Li to migrate between $\mathbf{H}_i$ and $\mathbf{O3}_i$/$\mathbf{O3}_{i+1}$ (T_{O3H}, blue routes in Figure 5) in the middle region (E_d = 0.00~0.49 eV); however, the migration

at the edge is not kinetically favored (green routes in Figure S2): the diffusion barriers from $\mathbf{O3_6}$ to $\mathbf{E_2}$ ($\mathbf{E_2}$ to $\mathbf{O3_6}$) and from $\mathbf{O3_1}$ to $\mathbf{H_1}$ ($\mathbf{H_1}$ to $\mathbf{O3_1}$) are 1.17 (1.07) and 1.02 (1.11) eV, respectively; Li migration from $\mathbf{O3_1}$ ($\mathbf{E_1}$) to $\mathbf{E_1}$ ($\mathbf{O3_1}$) has to overcome the energy barrier of 1.17 (0.74) eV in the edge plane; in sharp contrast, it only surpasses a barrier of 0.39 (0.01) eV for Li migrating from $\mathbf{E_2}$ ($\mathbf{E_3}$) to $\mathbf{E_3}$ ($\mathbf{E_2}$) in the edge plane. Compared to the big difference between the edge and middle region in T_{O3H} route (E_{d} = 0.00~1.17 eV), the energy barriers for Li migration from $\mathbf{O1}_i$ ($\mathbf{O1}_{i+1}$) to $\mathbf{O2}_i$ are in the range of 0.00~0.20 eV (0.00~0.01 eV), and the high energy barriers from $\mathbf{O2}_i$ to $\mathbf{O1}_i$ ($\mathbf{O1}_{i+1}$) are between 0.51 (0.25) and 0.60 (0.69) eV. We also examined the diffusing behavior in the T_{O3O2} pathways of $\mathbf{O3}_i\rightarrow\mathbf{O2}_i\rightarrow\mathbf{O3}_i$ and $\mathbf{O3}_{i+1}\rightarrow\mathbf{O2}_i\rightarrow\mathbf{O3}_{i+1}$ (i = 1−5), but the diffusion barriers are rather high in the range of 0.41~0.84 eV and 0.23~0.56 eV, respectively (Figure S3).

Clearly, Li prefers to diffuse along the periodic direction, which is different from the case of Li diffusion on MoS_2 ribbons,[6] but it can also diffuse in the transverse direction through the optimum path assuming Li atom adsorbs at the $\mathbf{O2_1}$ site where it has the binding energy of 3.50 eV: Li moves to $\mathbf{H_1}$ site (0.13 eV exothermic) by overcoming a barrier of 0.11 eV, followed by diffusion to $\mathbf{O3_2}$ site barrierlessly; then Li migrates through $\mathbf{O2_2}$, $\mathbf{O3_3}$, $\mathbf{O2_3}$, $\mathbf{O3_4}$, $\mathbf{H_4}$ and $\mathbf{O3_5}$ to reach $\mathbf{O2_5}$ site by surpassing barriers of 0.41, 0.33, 0.46, 0.39, 0.30, 0.01 and 0.42 eV, respectively, and each step is exothermic. The optimum path in the transverse direction and the corresponding energy profiles are illustrated in Figure 5.

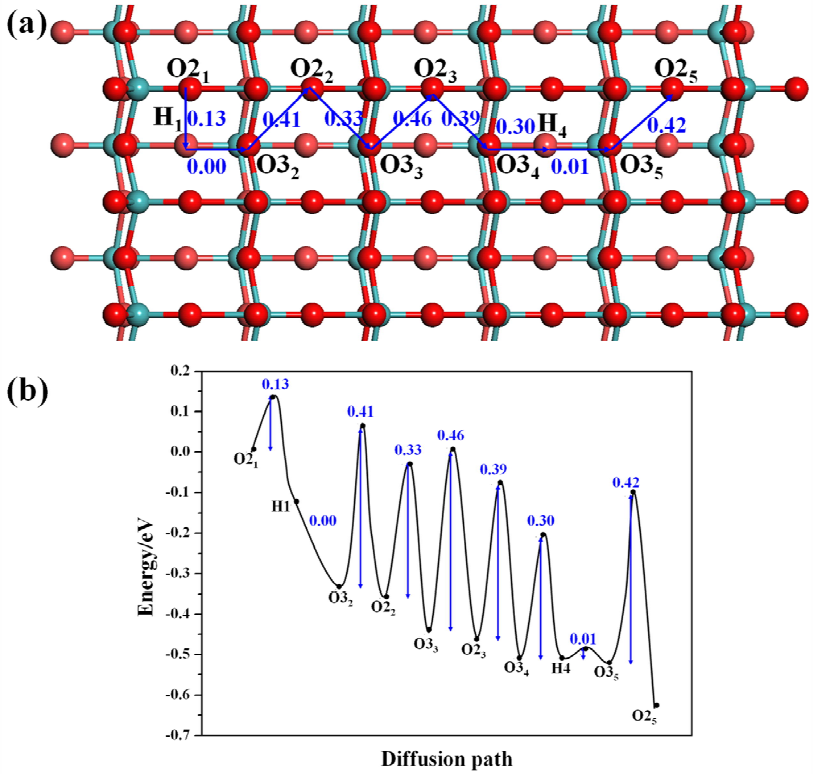

Figure 5. Top view (a) of Li diffusing across *12-c* MoO_3 NR along the transverse direction starting at **O2₁** site (its energy was set as zero), and the corresponding energy profiles (b). The numbers indicate the diffusion barriers in eV. The cyan (light cyan) and red (light red) balls denote Mo and atoms of one (the other) sublayer, respectively.

11-a NR.

We also explored the Li adsorption and diffusion behavior on *11-a* MoO_3 nanoribbon, since it has low edge formation energy.[36] More adsorption sites were involved, though it is symmetric, the structures of the two basal planes are different (Figure 6). The binding strength of Li on *11-a* nanoribbon is slightly stronger than that on *12-c* NR (Table 2): the Li binding energies at **O2** sites, **O3** sites, **H** sites, **O1** sites and **E** sites are in the range of 4.02~4.30, 4.08~4.20, 4.09~4.32, 3.60~3.70, and 3.44~4.30 eV, respectively. Among all the examined adsorption sites, **H₂₂** has the

largest E_b value (4.32 eV), which is 0.17 eV stronger than that of the energetically most favored site in bulk. The large Li binding energies indicate that the MoO_3 NRs possess high operating voltage.

However, it is not a local minimum on $\mathbf{H_1}$ site for Li adsorption – the Li atom on this site moved into the space between the two sublayers after full relaxation (marked as **In** site), and when being encapsulated in the edge region of *11-a* NR, Li binds with three O2 and two O3 oxygen atoms with the mean Li-O of 2.05 Å, while the binding energy (4.01 eV) is not enhanced compared to the surface adsorption. Besides, it is quite difficult for the encapsulated Li to diffuse between the two sublayers (the barrier is as high as 1.66 eV, see the pink route in Figure 7). These results may explain the recent experimental finding: the irreversible lithium insertion into the crystal structure, i.e., the MoO_3 intralayers, which tends to trigger unrecoverable structural transformation of α-MoO_3,[15,39] was found, which led to the lower cathodic peak (at 2.49 V).

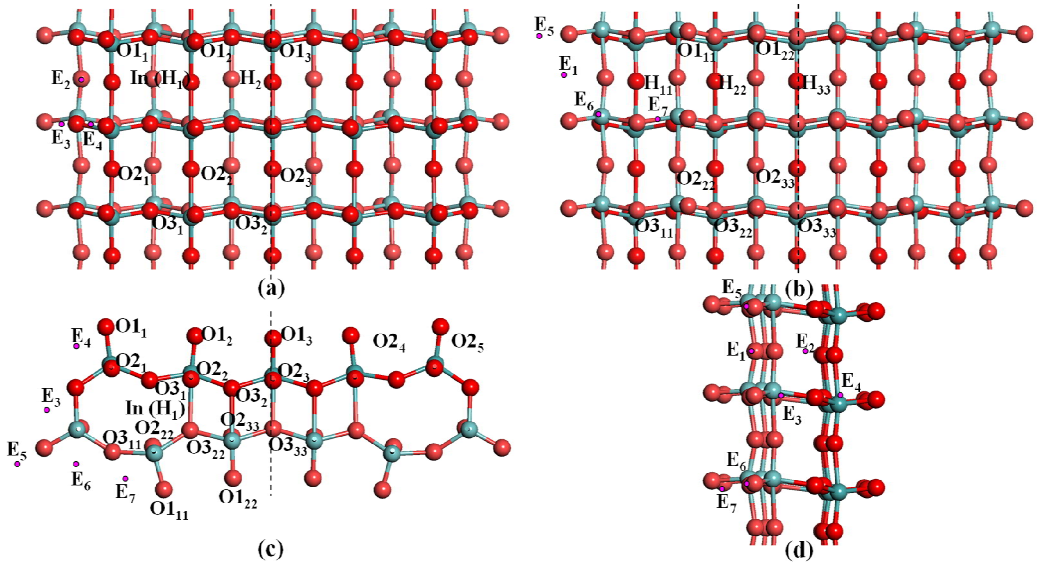

Figure 6. Top (a), bottom (b) and side (c, d) views of geometry of *11-a* MoO_3 NR. All the examined Li adsorption sites are denoted with black characters. The dashed lines represent the symmetric planes. The cyan (light cyan) and red (light red) balls denote Mo and atoms of one (the other) sublayer, respectively. The pink dots represent the edge adsorption sites.

Table 2. Computed Li binding energies (E_b) and average Li-O bond distances ($d_{Li\text{-}O}$) of all the examined Li adsorption sites for *11-a* MoO_3 NR.

Site	**H_1→In**	**H_2**	**H_{11}**	**H_{22}**	**H_{33}**		
E_b/eV	4.01	4.15	4.09	4.32	4.12		
$d_{Li\text{-}O}$/Å	2.05	2.18	1.96	2.15	2.18		
Site	**$O2_1$**	**$O2_2$**	**$O2_3$**	**$O2_{22}$**	**$O2_{33}$**		
E_b/eV	4.30	4.02	4.13	4.19	4.19		
$d_{Li\text{-}O}$/Å	1.97	2.02	2.04	2.03	2.28		
Site	**$O3_1$**	**$O3_2$**	**$O3_{11}$**	**$O3_{22}$**	**$O3_{33}$**		
E_b/eV	4.07	4.15	3.44	4.20	4.18		
$d_{Li\text{-}O}$/Å	1.88	1.88	1.94	1.86	1.88		
Site	**$O1_1$**	**$O1_2$**	**$O1_3$**	**$O1_{11}$**	**$O1_{22}$**		
E_b/eV	3.63	3.60	3.69	3.60	3.70		
$d_{Li\text{-}O}$/Å	1.74	1.77	1.76	1.76	1.76		
Site	**E_1**	**E_2**	**E_3**	**E_4**	**E_5**	**E_6**	**E_7**
E_b/eV	4.30	4.19	3.44	3.60	3.58	3.38	3.43
$d_{Li\text{-}O}$/Å	1.97	1.97	2.23	2.12	1.73	2.30	1.93

Similar to the case on *12-c* MoO_3 NR, the Li diffusion along periodic direction (P_{O3H}-i, i = 1−4; P_{O2O1}-i, i = 1−5; P_{InIn}; P_{E1E1}, P_{E3E3}, P_{E5E5}, P_{E1E5}, P_{E1E3}, P_{E1E5}, P_{E2E3}) and that along transverse direction on the basal plane (T_{O2H}, T_{O3O1}, T_{O2O3} and T_{O2O2}) and edge plane (T_{O2E2}, T_{E1E2}, T_{E3E4}, T_{O1E4}, T_{E3E5}, T_{H11E1}, T_{E5E6}, T_{E6E7}, T_{O1E7} and T_{O2E7}) were examined.

For Li diffusion along the periodic direction (as illustrated in Figure 7), it is kinetically favorable for Li to migrate through P_{O3H}-i (i = 1−3) channels (blue routes in Figure 7), the diffusion barriers are between 0.00 and 0.27 eV, and P_{O3H}-2 has the lowest diffusion barriers (0.00 and 0.06 eV) among the four P_{O3H} routes; moreover, the barriers of P_{O3H}-3 route (0.00 and 0.13 eV), where the $\mathbf{H_{22}}$ has the strongest Li binding energy, are reduced compared to the E_d values of similar diffusion route on MoO_3 monolayer (0.16 and 0.20 eV). However, the P_{O3H}-4 diffusion route is less kinetically favored due to the edge effect (the barriers are 0.12 and 0.77 eV); the energy barriers for Li diffusing from $\mathbf{O2}_i$ ($\mathbf{O2}_{ii}$) site to $\mathbf{O1}_i$ ($\mathbf{O1}_{ii}$) site (P_{O2O1}-i, i = 1−5) are in the range of 0.44~0.67 eV (black routes in Figure 7); the Li migration between two MoO_3 sublayers (P_{InIn}) is also energy-demanding (pink routes in Figure 7), the barrier is as high as 1.66 eV; the barriers of diffusing between edge sites in the periodic channels (P_{E1E1}, P_{E3E3}, P_{E5E5}, P_{E1E5}, P_{E1E3}, P_{E1E5}, P_{E2E3}) are higher than 0.71 eV (green routes in Figure 7).

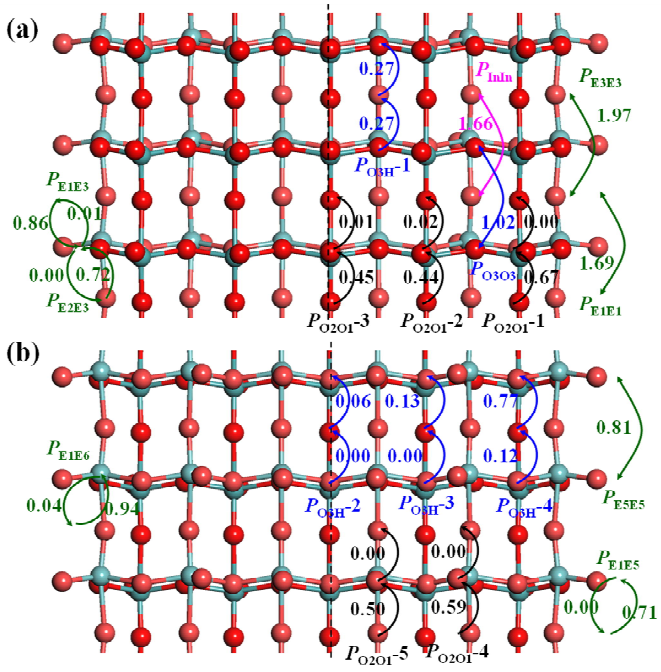

Figure 7. Top (a) and bottom (b) views of Li diffusion pathways on *11-a* MoO_3 NR along the periodic direction. The numbers indicate the diffusion barriers in eV. The cyan (light cyan) and red (light red) balls denote Mo and atoms of one (the other) sublayer, respectively.

Along transverse direction on *11-a* MoO_3 NR, the Li diffusion barriers of T_{O2H} routes on the both sublayers (blue routes in Figure 8) are relatively low (0.00~0.18 eV, except for the migration from $\mathbf{O2_{22}}$ to $\mathbf{H_{11}}$, which has to overcome a barrier of 0.79 eV); the barriers of Li diffusion between $\mathbf{O2_1}$ and $\mathbf{O2_2}$ are higher than 1 eV (T_{O2O2}, purple route in Figure 8); the barriers of Li migrating from $\mathbf{O3}_i$ ($\mathbf{O3}_{ii}$) to $\mathbf{O1}_i/\mathbf{O1}_{i+1}$ ($\mathbf{O1}_{ii}/\mathbf{O1}_{i+1i+1}$) are in the range of 0.44~0.60 eV (T_{O3O1}, black routes in Figure 8); among the transverse channels at the edge region, T_{H11E1}, T_{O2E2} and T_{E1E2} routes are less kinetically favored (the barriers are ~ 1 eV), while T_{E3E5}, T_{E5E6}, T_{E6E7}, T_{O1E4}, T_{O1E7} and T_{E3E4} has lower Li diffusion barriers (0.09~0.65 eV, green routes in Figure 8); the

Li diffusion barriers in the T_{O2O3} (0.30~0.70 eV) and T_{O2E7} (0.11, 0.87 eV) pathways are moderate (Figure S4).

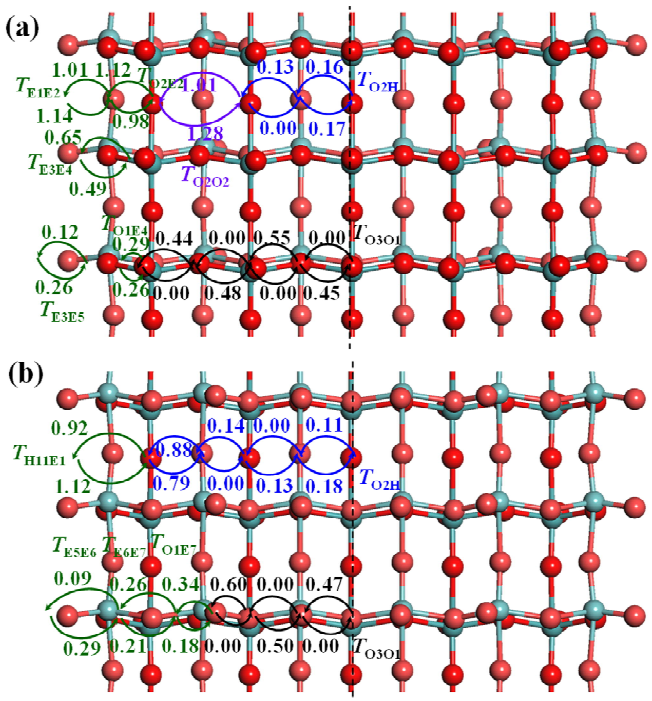

Figure 8. Top (a) and bottom (b) views of Li diffusion pathways on *11-a* MoO_3 NR along the transverse direction. The numbers indicate the diffusion barriers in eV. The cyan (light cyan) and red (light red) balls denote Mo and atoms of one (the other) sublayer, respectively.

Apparently, it is likely for Li to diffuse along the periodic direction on *11-a* MoO_3 NR, which is similar to the case on *12-c* NR. However, Li can also diffuse in the transverse direction through the optimum path starting from the central site $\mathbf{H_{33}}$ where it has the binding energy (4.12 eV) as shown in Figure 9: Li moves to $\mathbf{O2_{33}}$ site by overcoming a barrier of 0.11 eV, then barrier-free to $\mathbf{H_{22}}$ site.

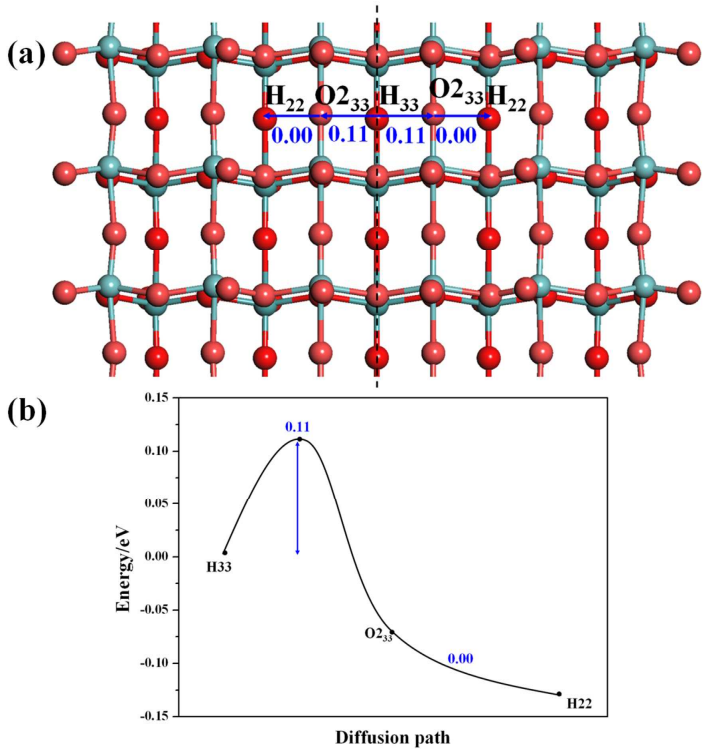

Figure 9. Top view (a) of Li diffusing across *11-a* MoO_3 NR along the transverse direction starting at **H_{33}** site (its energy was set as zero), and the corresponding energy profiles (b). The numbers indicate the diffusion barriers in eV. The cyan (light cyan) and red (light red) balls denote Mo and atoms of one (the other) sublayer, respectively.

3.3. Li storage capacity of MoO_3 bulk, double-layer, monolayer and NRs

We also estimated the Li storage capacity on MoO_3 nanostructures since Li adsorption and diffusion can result in Li accumulation.

Each unit cell of MoO_3 bulk, double-layer, monolayer, *11-a* and *12-c* NRs can accommodate up to four, six, four, 25 and 28 Li atoms (to avoid phase separation, the distance between any two adjacent Li atoms is larger than that in Li metal), which correspond to the chemical stoichiometry of MoO_3Li, $MoO_3Li_{1.5}$, MoO_3Li_2, $MoO_3Li_{2.27}$ and $MoO_3Li_{2.33}$, respectively. Accordingly, their theoretical Li storage

capacity is 186, 279, 372, 423 and 434 mA h g^{-1}, respectively. Obviously, it is the edge sites that contribute to higher Li capacity for NRs. The rather high average Li binding energies, 3.87, 3.44, 2.88, 3.03 and 3.06 eV for MoO_3 bulk, double-layer, monolayer, *11-a* and *12-c* NRs, respectively, indicate that these materials possess high operating voltage. Therefore, MoO_3 monolayer and nanoribbons can provide both high energy density and high open voltage as LIB cathode materials.

4. Conclusion

In summary, DFT computations were performed to investigate the Li intercalation and diffusion properties in MoO_3 bulk/double-layer and on MoO_3 monolayer/nanoribbons. Our comprehensive computations demonstrated that the Li mobility on MoO_3 monolayer can be remarkably increased compared with that in MoO_3 bulk/double-layer. Meanwhile, the Li binding energies on the MoO_3 monolayer are rather strong, though slightly weaker than that in bulk. Thus, MoO_3 monolayer is suitable for cathode applications. Cutting MoO_3 monolayer into 1D nanoribbons, both the binding strength and the mobility of Li atoms (by lowering the diffusion barrier) along the periodic direction can be further enhanced, particularly in the case of *11-a* NR; besides, Li can also migrate across the transverse direction on MoO_3 nanoribbons through the optimum paths, though the diffusion barriers are slightly higher than those along periodic direction. Both MoO_3 monolayer and NRs possess high operating voltage as well as high energy density. Moreover, the intercalation of lithium converts the semiconducting MoO_3 NRs into metals. These computations are helpful to understand and design MoO_3-based nanomaterials as the cathode materials for high-rate Li ion batteries.

Supporting Information

Band structures of MoO_3 pristine and Li-adsorbed *12-c* and *11-a* NRs, top view of Li diffusion T_{O3H} and T_{O2O1} pathways on *12-c* MoO_3 NR along the transverse direction, top view of Li diffusion pathways T_{O1H} and T_{O3O2} on *12-c* MoO_3 NR along the transverse direction, as well as top and bottom views of Li diffusion pathways T_{O2O3} and T_{O2E7} on *11-a* MoO_3 NR along the transverse direction.

Acknowledgment

Support by Department of Defense (Grant W911NF-12-1-0083) and by NSF (Grant EPS-1010094) is gratefully acknowledged. The project was partially funded by NASA-URC Grant Number NNX10AQ17A.

References

[1] M. Winter and R. J. Brodd, *Chem. Rev.*, 2004, **104**, 4245–4269.

[2] M. S. Whittingham, *Chem. Rev.*, 2004, **104**, 4271–4301.

[3] (a) W. Zhang, Y. Zeng, N. Xiao, H. H. Hng and Q. Yan, *J. Mater. Chem.*, 2012, **22**, 8455–8461. (b) X. Rui, Z. Lu, H. Yu, D. Yang, H. H. Hng, T. M. Lim and Q. Yan, *Nanoscale*, 2013, **5**, 556–560.

[4] Z. Wang, Q. Su and H. Deng, *Phys. Chem. Chem. Phys.*, 2013, **15**, 8705–8709.

[5] N. Margalit, *J. Electrochem. Soc.*, 1974, **121**, 1460–1461.

[6] Y. Li, D. Wu, Z. Zhou, C. R. Cabrera and Z. Chen, *J. Phys.Chem. Lett.*, 2012, **3**, 2221–2227.

[7] H. Zhong, G. Yang, H. Song, Q. Liao, H. Cui, P. Shen and C. Wang, *J. Phys. Chem. C*, 2012, **116**, 9319–9326.

[8] Y. Jing, Z. Zhou, C. R. Cabrera, Z. Chen, Graphene, Inorganic Graphene Analogs and Their Composites for Lithium Ion Batteries, *J. Mater. Chem. A.* 2014, **2**, 12104-12122.

[9] (a) H. Brakken, *Z. Krist*, 1931, **78**, 484. (b) N. Wooster, *Z. Krist*, 1931, **80**, 504–512.

[10] T. Tsumura and M. Inagaki, *Solid State Ionics*, 1997, **104**, 183–189.

[11] W. Y. Li, F. Y. Cheng, Z. L. Tao and J. Chen, *J. Phys. Chem. B*, 2006, **110**, 119–124.

[12] T. A. Kerr, H. Wu and L. F. Nazar, *Chem. Mater.*, 1996, **8**, 2005–2015.

[13] C. V. S. Reddy, E. H. Walker Jr., C. Wen and S. Mho, *J. Power Sources*, 2008, **183**, 330–333.

[14] (a) L. Q. Mai, B. Hu, W. Chen, Y. Y. Qi, C. S. Lao, R. S. Yang, Y. Dai and Z. L. Wang, *Adv. Mater.*, 2007, **19**, 3712–3716. (b) C. V. S. Reddy, Z. R. Deng, Q. Y. Zhu, Y. Dai, J. Zhou, W. Chen and S.-I. Mho, *Appl. Phys. A* 2007, **89**, 995 – 999.

[15] J. S. Chen, Y. L. Cheah, S. Madhavi and X. W. Lou, J. Phys. Chem. C, 2010, **114**, 8675–8678.

[16] W. C. West and J. F.Whitacre, *J. Electrochem. Soc.,* 2005, **152**, A966–A969.

[17] K. Dewangan, N. N. Sinha, P. K. Sharma, A. C. Pandey, N. Munichandraiah and N. S. Gajbhiye, *CrystEngComm* 2011, **13**, 927–933.

[18] L. Zhou, L. C. Yang, P. Yuan, J. Zou, Y. P. Wu and C. Z. Yu, *J. Phys. Chem. C*, 2010, **114**, 21868–21872.

[19] U. K. Sen and S. Mitra, *RSC Advances*, 2012, **2**, 11123–11131.

[20] B. Mendoza-Sánchez and P. S. Grant, *Electrochimica Acta*, 2013, **98**, 294–302.

[21] S. H. Lee, Y. H. Kim, R. Deshpande, P. A. Parilla, E. Whitney, D. T. Gillaspie, K. M. Jones, A. H. Mahan, S. B. Zhang and A. C. Dillon, *Adv. Mater.*, 2008, **20**, 3627–3632.

[22] M. A. Ibrahem, F. Wu, D. A. Mengistie, C. Chang, L. Li and C. W. Chu, *Nanoscale*, 2014, **6**, 5484–5490.

[23] P. Meduri, E. Clark, J. H. Kim, E. Dayalan, G. U. Sumanasekera and M. K. Sunkara, *Nano Lett.* 2012, **12**, 1784–1788.

[24] M. Hassan, Z. Guo and Z. Chen, *J. Power Sources*, 2010, **195**, 2372–2376.

[25] C. Julien, G. A. Nazri, J. P. Guesdon, A. Gorenstein, A. Khelfa and O. M. Hussain, *Solid State Ionics*, 1994, **73**, 319−326.

[26] S. M. Jolanta, *J. Phys. Chem. C*, 2008, **112**, 11050–11058.

[27] Q. Tang, Z. Zhou and P. Shen, *J. Am. Chem. Soc.*, 2012, **134**, 16909−16916.

[28] D. Wu, Y Li and Z. Zhou, *Theor. Chem. Acc.*, 2011, **130**, 209−213.

[29] J. Bao, D. Wu, Q. Tang, Z. Ma and Z. Zhou, *Phys. Chem. Chem. Phys.*, 2014, **16**, 16145−16149.

[30] X. Tan and Z. Chen, *J. Phys. Chem. C*. 2014, **DOI:** 10.1021/jp503597n

[31] Y. Jing, Z. Zhou, C. R. Cabrera and Z. Chen, *J. Phys. Chem. C.* 2013, **117**, 25409–25413.

[32] Q. Tang and Z. Zhou, *Prog. Mater. Sci.*, 2013, **58**, 1244−1315.

[33] Y. Jing, Z. Zhou, C. R. Cabrera and Z. Chen, *J. Mater. Chem. A*. 2014, **2**, 12104-12122.

[34] Y. Liu, V. I. Artyukhov, M. Liu, A. R. Harutyunyan and B. I. Yakobson, *J. Phys. Chem. Lett.*, 2013, **4**, 1737−1742.

[35] C. Uthaisar, V. Barone and J. E. Peralta, *J. Appl. Chem.*, 2009, **106**, 113715.

[36] F. Li and Z. Chen, *Nanoscale*, 2013, **5**, 5321–5333.

[37] M. Baldoni, L. Craco, G. Seifert and S. Leoni, *J. Mater. Chem. A*, 2013, **1**, 1778–1784.

[38] J. M. Tarascon and M. Armand, *Nature*, 2001, **414**, 359−367.

[39] W. Y. Li, F. Y. Cheng, Z. L. Tao and J. Chen, *J. Phys. Chem. B*, 2006, **110**, 119–124.